Supplementary information for

Dynamic and Reversible Shape Response of Red Blood Cells in Synthetic Liquid Crystals

Karthik Nayani[a], Arthur A. Evans[b], Saverio E. Spagnolie[b], and Nicholas L. Abbott[a,1]

[a] Smith School of Chemical and Biomolecular Engineering, Cornell University, Ithaca, NY, USA

[b] Department of Mathematics, University of Wisconsin - Madison, Madison, WI, USA

[1] To whom correspondence should be addressed. Email: nabbott@cornell.edu.

This PDF file includes:

Other supplementary materials for this manuscript include the following:

Supplementary Information Text

Materials and Methods

Materials:

Healthy human RBCs were purchased from Innovative Research Inc (Novi, MI). The RBCs were ultracentrifuged and then re-dispersed in isotonic solutions of NaCl (154 mM). To prepare RBCs in 17.3 wt% DSCG, 1 vol% of the RBCs in isotonic NaCl solutions were pipetted into DSCG solutions. The resulting mixtures were gently vortexed. The membrane staining dye 1, 1' dioctadecyl-3, 3, 3', 3' tetramethylindodicarbocyanine, 4-chlorobenezenesulfonate salt (DiD) was purchased from Avanti Polar Lipids, Inc. (Alabaster, AL) and used to stain RBCs for confocal scanning microscopy. DSCG was purchased from Sigma-Aldrich (Milwaukee, WI). Fisher's Finest Premium grade glass slides and cover glass were purchased from Fisher Scientific (Pittsburgh, PA). Deionization of a distilled water source was performed with a Milli-Q system (Millipore, Bedford, MA) to give water with a resistivity of 18.2 MΩ cm.

Preparation of Optical Cells:

Solutions of polyimide (PI2555, HD MicroSystems) were spin-coated onto glass microscope slides following the manufacturer's instructions. The cured films were mechanically sheared by rubbing along a given direction with a velvet cloth to create surfaces that induced planar alignment of nematic DSCG solutions. Two polyimide-coated glass substrates were paired (parallel directions of rubbing) and spaced apart by 100 μm using double-sided tape to create a cavity into which a volume (~2 μL) of DSCG solution containing dispersed RBCs was drawn by capillarity. After filling, each optical cell was immediately sealed with silicone grease to prevent evaporation of water. All measurements reported in this paper were performed with optical cells with thicknesses of 100 μm, except for measurements performed with the Polscope. For Polscope measurements, we used optical cells with thicknesses of 20 μm. The use of thin optical cells in Polscope measurements enabled us to map the LC orientation close to the surface of the RBC (as it minimized the contribution of LC above and below the RBC, along the z-axis, to the optical retardance map).

Optical Microscopy:

RBCs dispersed in 17.3 wt% DSCG and isotonic NaCl solutions were imaged using an Olympus BX60 upright microscope equipped with 60× and 50× objectives, crossed polarizers, and a 100W mercury lamp. Images were captured using a digital camera (Olympus C-2040 Zoom) mounted on the microscope and set to a f-stop of 2.8 and a shutter speed of 1/15 s.

Confocal Fluorescence Microscopy:

The 3-D rendering of the strained RBC shapes was obtained using a Carl Zeiss LSM 700 laser confocal scanning microscope. The RBCs were dispersed in isotonic NaCl solutions and stained with a membrane staining dye (DiD) at concentrations of 15 μM for a period of 3 hrs at a temperature of 30°C. Stained cells were then ultra-centrifuged and washed in isotonic NaCl solutions twice before dispersing them in DSCG solutions. 63X water immersion objectives were used to obtain the z-stack images of strained RBCs. Zen Blue software was in imaging the strained RBCs and 3-D viewer plugin of Fiji software was employed for constructing the 3-D render of the RBCs. Values of r_y obtained from optical micrographs of RBCs were used as a reference for determining the threshold values of the 3-D viewer plugin in Fiji. The values of r_z were then obtained from the

cross-section of the 3-D shape rendered by the 3D viewer plugin.

Vapor pressure Osmometry:

A VAPRO 5520 vapor pressure osmometer (Logan, UT) was used to measure the osmotic pressures of aqueous DSCG at different concentrations. The measurements were compared with a 154 mM NaCl solution (as a reference) measured using the same instrument. The averages presented in Figure 2 of the main text were obtained from four independent measurements.

Imaging RBCs dispersed in isotonic NaCl and 17.3% DSCG solutions:

Figure S1(A) shows an optical micrograph of healthy RBCs dispersed in an aqueous solution of 154 mmol NaCl that is isotonic with the RBC interior. Under these conditions, we observed the RBCs to retain their biconcave shape for several hours. Figure S1(B) shows a micrograph of RBCs dispersed in a nematic phase of 17.3% DSCG. This representative image shows about 60 cells, which were analyzed to quantify their aspect ratio, r_x/r_y (see main text).

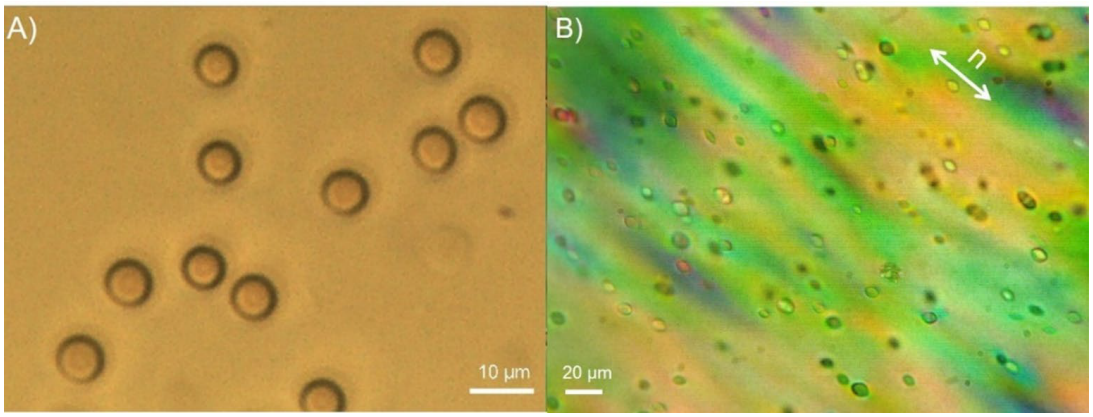

Figure S1: Optical micrograph of RBCs. (a) RBCs in isotropic aqueous 154 mM NaCl. (B) RBCs in nematic 17.3% aqueous DSCG at 25°C.

Polscope measurement of LC orientation around a RBC:

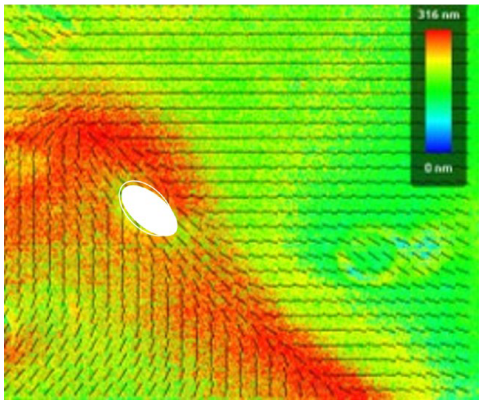

Figure S2: Polscope map of LC director profile around a RBC dispersed in 17.3% aqueous DSCG.

To quantify the orientation of the LC around an individual RBC, we used a Polscope. Polscope imaging was performed using an Olympus BX41 microscope equipped with an Abrio LC-PolScope and monochromatic illumination at 640 nm. Figure S2 shows a RBC near a $+1/2$ defect and the Polscope mapping of the director profiles around the RBC. The $+1/2$ defect was used to confirm the fidelity of the mapping of the director profile. The director profile of the LC around the RBC (shown as a white ellipsoid) in Figure S2 is consistent with a preferred tangential orientation of the LC near the surface of the RBC, although the distortion is weak and thus consistent with weak anchoring of the LC.

Z-stacks of strained RBCs obtained by confocal microscopy:

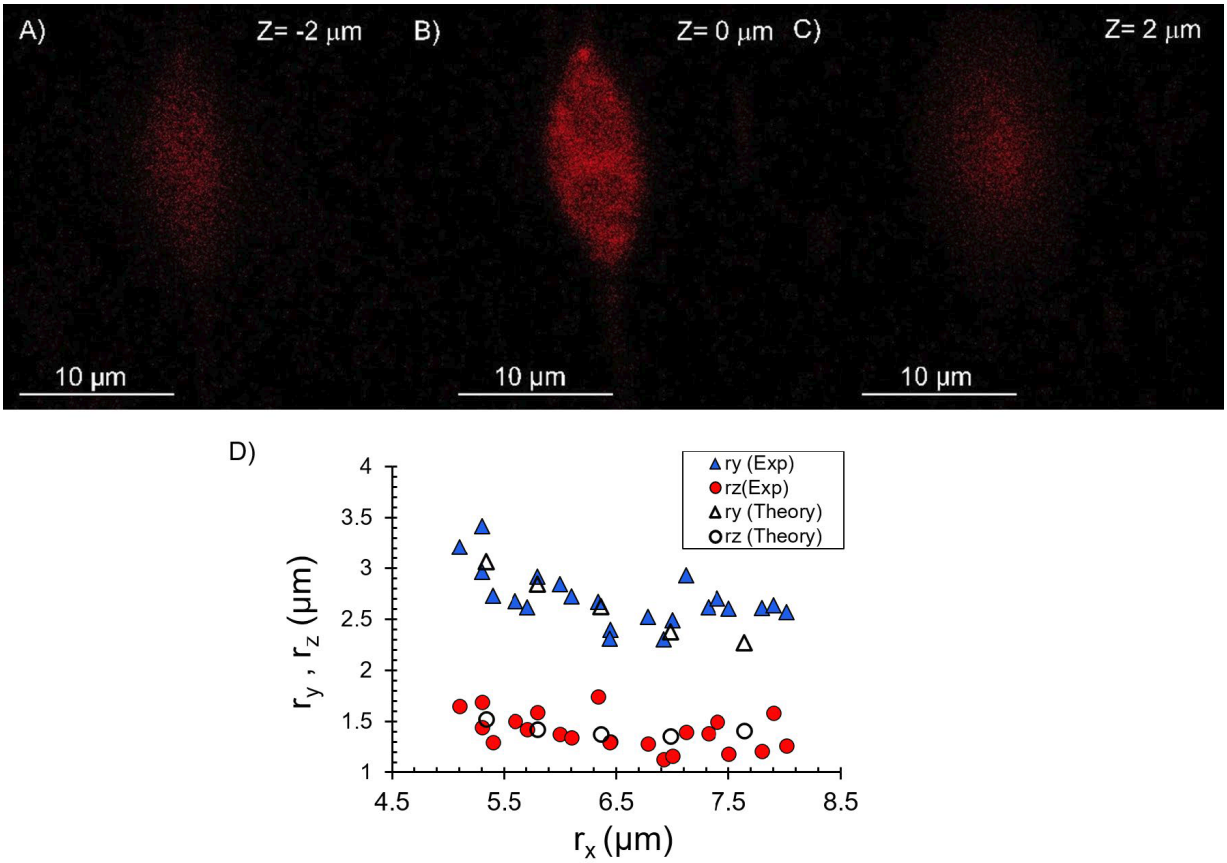

Figure S3: A) through C) Confocal fluorescence micrographs at three different z-planes of a strained RBC dispersed in aqueous 17.3% DSCG D) Plot of individual measurements of r_x, r_y and r_z. All measurements were performed at 25°C.

Movie M1 shows a 3-D reconstruction of a z-stack of images of RBCs obtained by using confocal microscopy. 3-D viewer plugin in Fiji software (threshold = 15) was used to obtain the 3-D rendering of the strained RBC dispersed in a nematic phase of DSCG. Figure S3 shows three of the z-stack images (12, in total), either at the mid-plane or 2 μm.

A number of observations establish that the large aspect ratios measured for strained RBCs are not the result of characterizing unstrained biconcave RBCs viewed from the side: 1) 3-D reconstructions of the confocal micrographs confirm that all RBCs strained in LCs have an elongated and folded shape with a non-circular cross-section (see Figure 4 of main text); 2) We cross-

linked strained cells and redispersed them in water, as presented in Figure 5A. Images of the cross-linked cells confirmed that the cells were elongated and folded in shape; 3) If RBCs with biconcave shapes were viewed side-on, the aspect ratio would be ~ 4. However, as shown in Figure 3C, the aspect ratios measured in our experiments were typically around 2, with the largest being 3.4.

Figure 4D shows r_y/r_z plotted as a function of r_x/r_y, revealing r_y/r_z varies little between cells (1.9 ± 0.2) while r_x/r_y varies substantially. We provide the individual values of r_x, r_y and r_z (μm) in Figure S3D.

RBCs cross-linked with glutaraldehyde:

Figure S4 shows RBCs that were cross-linked with glutaraldehyde and re-dispersed in 17.3% aqueous DSCG. Unlike healthy RBCs, we do not observe cross-linked RBCs to undergo shape-changes induced by the elasticity of the LC.

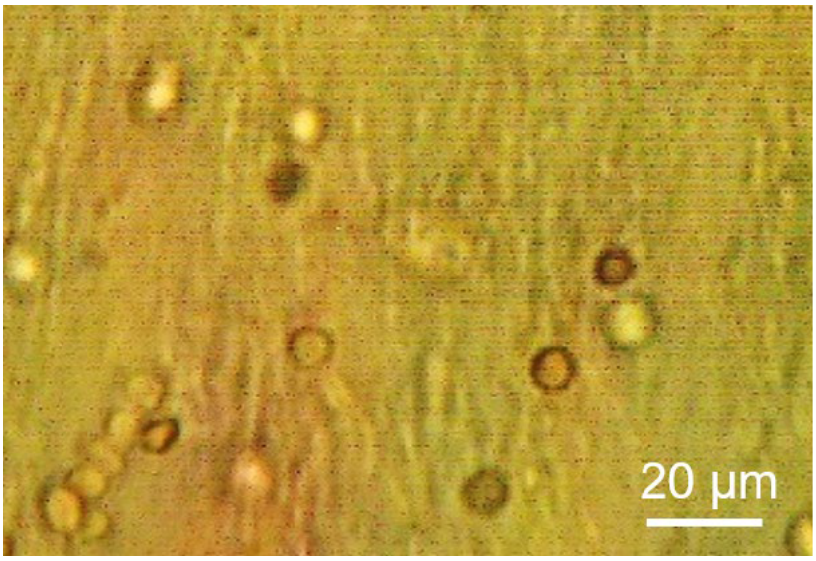

Figure S4: RBCs cross-linked with glutraldehyde and re-dispsersed in nematic 17.3% aqueous DSCG

Reversible shape transitions of RBCs:

Figure S5 shows reversible shape transformations of RBCs, from elongated shapes to biconcave shapes, as they move from nematic regions of the aqueous DSCG into isotropic domains in the biphasic regime of the phase diagram.

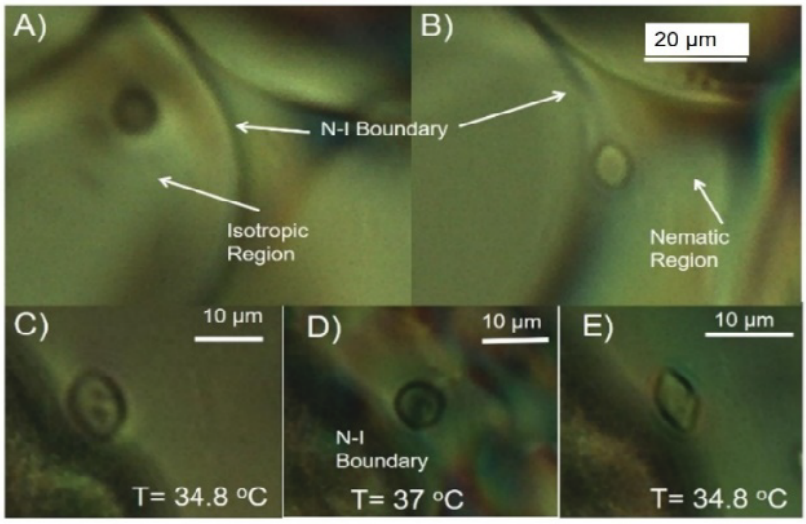

Figure S5: A and B) Optical micrographs showing shapes of RBCs in the isotropic and nematic domains of the biphasic region of 17.3% DSCG, respectively C)-E) Reversible shape changes of an RBC as it is exposed sequentially to nematic (C) isotropic (D) and nematic (E) phases. Samples were heated at 1°C/min.

Shriveling of RBCs in the isotropic phase:

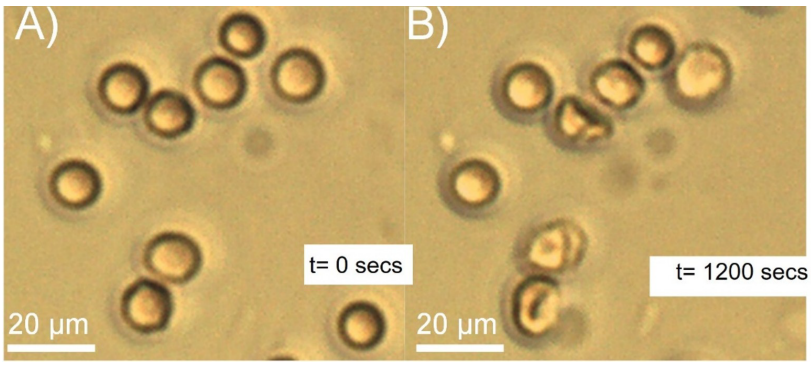

Figure S6: (A) Optical micrograph showing biconcave shape of RBC immediately following dispersal into isotropic phase of 17.3 wt% DSCG at temperature of T = 39°C. B) Shriveled shapes of RBCs after 1200 secs.

We note that changes in the temperature of DSCG solutions, which lead to RBC shape changes of the type shown in Figure S5, are accompanied by changes in LC elasticity as well as osmotic pressure. The change in osmotic pressure with temperature underlies the observation that RBCs dispersed in 17.3 wt% DSCG solution, when heated to 39°C (an isotropic and hypertonic phase), show evidence of shriveling after 20 minutes (Figure S6). The time-scale (>20 mins) associated with the shriveling of RBCs, however, allowed us to eliminate the possibility that the reversible shape changes of RBCs upon cycling between the

nematic and isotropic domains, as shown in Figure S5, are a result of osmotic stresses. Specifically, the RBC shape changes (biconcave disks in isotropic; elongated shapes in nematic) can be observed within a few seconds of the phase transition between the isotropic and LC phases, thus revealing that the timescales associated with the changes of RBC shape due to the LC elasticity ($\sim$ secs) and the shape changes due induced by osmotic pressure ($\sim$ 20 mins) are decoupled in time. The experimentally observed changes of aspect ratios as a function of temperature were obtained at a heating rate of 5°C/min and equilibrating the sample at a given temperature for 30s. We conclude that the RBC shape changes that we report as a function of temperature in this paper are the result of changes in LC elasticity and not changes in osmotic pressure.

Mathematical model:

We describe the orientational order of the LC by a second-rank order tensor $\mathbf{Q}(\boldsymbol{x}, t)$ (Landau-de Gennes model) with $\boldsymbol{x} \in \mathbb{R}^3$ denoting the spatial position and t denoting time. In a uniaxial system, as assumed here, we write $\mathbf{Q} = S(\boldsymbol{nn} - \mathbf{I}/3)$, where S is the Maier-Saupe scalar order parameter, $\boldsymbol{n}$ is the director field (with $|\boldsymbol{n}(\boldsymbol{x}, t)| = 1$), $\boldsymbol{nn}$ is a dyadic product, and $\mathbf{I}$ is the identity operator [1, 2]. Following Refs. [3, 4], the total free energy $\mathcal{F}$ associated with $\mathbf{Q}$ is a combination of both short-range ($\mathcal{F}_S$) and elastic ($\mathcal{F}_E$) contributions over the fluid domain Ω,

$$\mathcal{F} = \mathcal{F}_S + \mathcal{F}_E, \tag{1}$$

$$\mathcal{F}_S = \int_\Omega f_S(\mathbf{Q})\, dv, \quad \mathcal{F}_E = \int_\Omega f_E(\mathbf{Q}, \nabla\mathbf{Q})\, dv, \tag{2}$$

with dv an infinitessimal volume element. The short-range energy density is given by

$$f_S(\mathbf{Q}) = \frac{A}{2}\left(1 - \frac{U}{3}\right)\mathrm{tr}\left(\mathbf{Q}^2\right) - \frac{AU}{3}\mathrm{tr}\left(\mathbf{Q}^3\right) + \frac{AU}{4}\mathrm{tr}\left(\mathbf{Q}^2\right)^2, \tag{3}$$

where A is an energy scale for the phase transition and U is a dimensionless nematic strength. The bulk scalar order parameter describing the LC when undisturbed by the RBC's presence is given by

$$S = \frac{1}{4} + \frac{3}{4}\sqrt{1 - \frac{8}{3U}}, \tag{4}$$

and the system is in the nematic phase when $U > 2.8$. The elastic energy density is given by

$$f_E(\mathbf{Q}, \nabla\mathbf{Q}) = \frac{L_1}{2}(\nabla\mathbf{Q})^2 + \frac{L_2}{2}(\nabla \cdot \mathbf{Q})^2 + \frac{L_3}{2}\mathbf{Q} : (\nabla\mathbf{Q} : \nabla\mathbf{Q}), \tag{5}$$

where in terms of the Frank constants $\{K_1, K_2, K_3\}$, we have $L_1 = (3K_2 - K_1 + K_3)/(6S^2)$, $L_2 = (K_1 - K_2)/S^2$, and $L_3 = (K_3 - K_1)/(2S^2)$. We set $L_3 = 0$, which specifies the bend and splay Frank elastic constants to be equal in magnitude ($K_1 = K_3$), while K_2 is an order of magnitude smaller.

The order tensor evolves due to stresses associated with the above energies as well as velocity gradients. Since we are seeking equilibrium shapes, we consider an artificially small rotational viscosity ($\gamma \ll 1$), which provides a separation of time-scales between director-field relaxation and fluid flow. In this limit, for a membrane shape at any moment in time the $\mathbf{Q}$ tensor first

relaxes to equilibrium following

$$\frac{\partial \mathbf{Q}}{\partial t} = -\frac{1}{\gamma}\mathbf{H}, \tag{6}$$

until $\mathbf{H} = 0$, where $\mathbf{H}$ is the symmetric and traceless part ($[...]^{ST}$) of the variational derivative of the free energy with respect to $\mathbf{Q}$,

$$\mathbf{H} = \left[\frac{\delta \mathcal{F}}{\delta \mathbf{Q}}\right]^{ST} = -L_1\nabla^2\mathbf{Q} - L_2[\nabla(\nabla\cdot\mathbf{Q})]^{ST} + A\left(1-\frac{U}{3}\right)\mathbf{Q} - AU\left(\mathbf{Q}^2 - \mathrm{tr}\left(\mathbf{Q}^2\right)\left(\mathbf{Q}+\frac{1}{3}\mathbf{I}\right)\right). \tag{7}$$

This relaxation must also incorporate the boundary conditions on the surface of the blood cell, denoted by $\partial\Omega$, which are captured by an additional surface energy,

$$\mathcal{F}_B = \int_{\partial\Omega} f_B[\mathbf{Q}(\boldsymbol{X}(\boldsymbol{S}))]\, dA, \tag{8}$$

where the boundary $\partial\Omega$ is parameterized as $\boldsymbol{X}(\boldsymbol{S})$ (suppressing the time-dependence) with infinitesimal surface area element dA. The surface energy is incorporated into the boundary conditions in the style of the Immersed Boundary method [5, 6]. The tensor $\mathbf{Q}(\boldsymbol{X}(\boldsymbol{S}))$ is an interpolation from the bulk LC onto the boundary using a bulk-to-surface interpolation operator $\mathcal{S}^*$, defined (along with $\mathcal{S}$, a surface-to-bulk spreading operator) as

$$\mathcal{S}^*[\mathbf{Q}](\boldsymbol{X}(\boldsymbol{S})) = \int_\Omega \mathbf{Q}(\boldsymbol{x})\delta(\boldsymbol{x}-\boldsymbol{X}(\boldsymbol{S}))dv, \tag{9}$$

$$\mathcal{S}[\mathbf{Q}](\boldsymbol{x}) = \int_{\partial\Omega} \mathbf{Q}(\boldsymbol{X}(\boldsymbol{S}))\delta(\boldsymbol{x}-\boldsymbol{X}(\boldsymbol{S}))dA, \tag{10}$$

where δ is the Dirac delta function with support confined to the surface of the RBC, $\boldsymbol{x} \in \partial\Omega$. Deviations from a tangential orientation of the LC on the surface of the RBC are penalized with a Rapini-Papoular surface energy density of the form

$$f_B(\mathbf{Q}) = \frac{J}{2}\mathrm{tr}\left(\mathbf{Q} - \mathbf{Q}^0(\boldsymbol{X}(\boldsymbol{S}))\right)^2, \tag{11}$$

where $\mathbf{Q}^0$ is the projection of $\mathbf{Q}$ onto the local tangent plane (the plane orthogonal to the unit normal vector at $\boldsymbol{X}(\boldsymbol{S})$, denoted by $\boldsymbol{N}$), $\mathbf{Q}^0 = (\mathbf{I} - \boldsymbol{N}\boldsymbol{N})\cdot\mathcal{S}^*[\mathbf{Q}]$, and J is an anchoring strength. The inclusion of $\mathcal{F}_B$ in the variational derivative of the energy results in replacing the molecular field in Eq. (7) (still with $\mathcal{F} = \mathcal{F}_S + \mathcal{F}_E$) by

$$\mathbf{H} = \left[\frac{\delta \mathcal{F}}{\delta \mathbf{Q}}\right]^{ST} + J\mathcal{S}\left[\mathcal{S}^*[\mathbf{Q}] - \mathbf{Q}^0\right], \tag{12}$$

in order to advance $\mathbf{Q}$ everywhere in space with no special gridpoints or other adaptive numerical machinery. The reactive component of the stress is divided into the Ericksen stress $\boldsymbol{\sigma}^E$ and the Landau-de Gennes stress denoted by the coupling $\mathbf{H} : \boldsymbol{\lambda}$, where again using the symmetry of $\mathbf{Q}$,

$$\boldsymbol{\sigma}^E = -\frac{\partial f_e}{\partial \nabla\mathbf{Q}} : \nabla\mathbf{Q} = -L_1\nabla\mathbf{Q} : \nabla\mathbf{Q} - L_2\nabla\mathbf{Q}\cdot(\nabla\cdot\mathbf{Q}), \tag{13}$$

$$\mathbf{H} : \boldsymbol{\lambda} = 2\mathbf{H}\cdot\mathbf{Q} + \frac{1}{3}\frac{I}{\Delta I}\mathbf{H} - \left(1+\frac{1}{2}\frac{I}{\Delta I}\right)\mathrm{tr}\,(\mathbf{H}\cdot\mathbf{Q})\,\mathbf{Q}. \tag{14}$$

The molecular parameter $I/\Delta I$ describes the shape of the underlying molecules, with $I/\Delta I = 2$ for an infinitely slender rodlike molecule; for a prolate, rodlike liquid crystal such as 5CB, $I/\Delta I \approx 1$ [3, 4], and for the remainder we fix $I/\Delta I = 1$.

The Rapini-Papoular formulation of the anchoring energy in Eq. (11) (second order in $\mathbf{Q}$) is a less accurate description of degenerate planar anchoring than the Fournier-Galatola formulation (fourth order in $\mathbf{Q}$) [7]. We did not adopt the Fournier-Galatola formulation because the additional nonlinearities so introduced created challenges related to numerical convergence. Similar to the findings in Ref. [8], the results generated by our numerical simulations agree closely with the experimental observations, suggesting that our use of the Rapini-Papoular formulation of the anchoring energy is a reasonable approximation in this setting.

Surface forces and evolution:

The deformation energy of the red blood cell is described by the Skalak model [9, 10], as detailed by Zhao et al. [11] (see also Refs. [12–15]). In the Skalak model, the RBC membrane is assumed to be an isotropic and hyperelastic surface, with a strain energy potential which depends on its deformation away from an initial biconcave configuration. The strain energy potential can be written in terms of the invariants of the surface strain tensor (the strain invariants), described below. Membrane near-inextensibility enters into the model via a large area dilation modulus.

Given a reference surface configuration denoted by $\boldsymbol{X}_0$ and current configuration $\boldsymbol{X}(\boldsymbol{X}_0, t)$ at time t, we define the surface deformation gradient tensor

$$\mathbf{F} = (\mathbf{I} - \boldsymbol{N}\boldsymbol{N}) \cdot \frac{\partial \boldsymbol{X}}{\partial \boldsymbol{X}_0} \cdot (\mathbf{I} - \boldsymbol{N}_0\boldsymbol{N}_0), \tag{15}$$

where $\boldsymbol{N}_0$ is the outward-pointing normal in the reference configuration and $\boldsymbol{N}$ is the same but in the current configuration; from this deformation gradient tensor we define $\mathbf{b} = \mathbf{F} \cdot \mathbf{F}^T$, the symmetric surface left Cauchy-Green strain tensor. The invariants of this tensor (the strain invariants) are

$$I_1 = \lambda_1^2 + \lambda_2^2 - 2, \tag{16}$$

$$I_2 = \lambda_1^2\lambda_2^2 - 1. \tag{17}$$

The Skalak strain energy of a surface area element dA is given by

$$W\, dA = \left(\frac{E_S}{4}\left[I_1^2 + 2I_1 - 2I_2\right] + \frac{E_D}{8}I_2^2\right) dA, \tag{18}$$

where E_S and E_D are the (constant) elastic shear and area dilation moduli, respectively, and have units of energy per area. The in-plane Cauchy stress tensor is given by

$$\boldsymbol{\tau} = \frac{2}{\lambda_1\lambda_2}\frac{\partial W}{\partial I_1} + 2\lambda_1\lambda_2\frac{\partial W}{\partial I_2}(\mathbf{I} - \boldsymbol{N}\boldsymbol{N}) = \frac{E_S}{2\mathcal{J}}(I_1 + 1)\mathbf{b} + \frac{\mathcal{J}}{2}(E_D I_2 - E_S)(\mathbf{I} - \boldsymbol{N}\boldsymbol{N}), \tag{19}$$

where $\mathcal{J} = \lambda_1\lambda_2$ measures the local area dilatation. We take $E_S = 4.2 * 10^{-6}$N/m and $E_D = 10^{-4}$N/m following Refs. [10–12]. The surface force density, $\boldsymbol{f}(\boldsymbol{X}(\boldsymbol{X}_0, t))$, is found by functional variation of the total surface energy with respect to the position variable.

For a reference configuration we take the initial shape described in Ref. [12]. Parameterizing the surface with angles $\chi \in [-\pi/2, \pi/2)$ and $\phi \in [0, 2\pi)$, we write

$$\boldsymbol{X}_0(\chi, \phi) = a \sin\chi \cos\phi\, \hat{\mathbf{x}} + a \sin\chi \sin\phi\, \hat{\mathbf{y}} + \frac{a}{2}\left(0.207 + 2.003 \sin^2\chi - 1.123 \sin^4\chi\right)\cos\chi\, \hat{\mathbf{z}}, \tag{20}$$

where a is the cell radius ($a \approx 4\,\mu$m). To provide an approximately uniform spatial coverage we use *Distmesh* [16] to generate a triangulated mesh of the surface above, shown in Figure 5 of the main text. Numerically, we use the deformation of each triangular element to extract the surface deformation gradient tensor and the principal stretches λ_1 and λ_2 on each triangle. Finite difference approximation of the variation in energy with displacement of each grid-point is performed to identify the surface force $\mathbf{f}$.

Non-dimensionalization:

We scale lengths upon the RBC radius a, forces by L_1, velocities by $L_1/(a\mu)$, time by $a^2\mu/L_1$, and energies by aL_1. The dimensionless molecular field is then given by

$$\mathbf{H} = -\nabla^2\mathbf{Q} - \bar{L}_2[\nabla(\nabla\cdot\mathbf{Q})]^{ST} + \beta^2\left(1 - \frac{U}{3}\right)\mathbf{Q} - \beta^2 U\left(\mathbf{Q}^2 - \mathrm{tr}\left(\mathbf{Q}^2\right)\left(\mathbf{Q} + \frac{1}{3}\mathbf{I}\right)\right) + \bar{J}\mathcal{S}[\mathcal{S}^*[\mathbf{Q}] - \mathbf{Q}^0], \tag{21}$$

where

$$\beta^2 = \frac{Aa^2}{L_1} = \left(\frac{a}{\xi_N}\right)^2, \quad \bar{J} = \frac{Ja}{L_1} = \frac{a}{\xi_S}, \quad \bar{L}_2 = \frac{L_2}{L_1}\cdot \tag{22}$$

Here we have also defined the nematic coherence length $\xi_N = (L_1/A)^{1/2}$ and the extrapolation length $\xi_S = L_1/J$. Typical values for the bulk free energy parameters in DSCG are given by $A \approx 400\,\mathrm{J\ m^{-3}}$ (two orders of magnitude smaller than for 5CB, for which $A \approx 10^5 J/m^3$ [8]), $L_1 \approx 10^{-12}\mathrm{J\ m^{-1}}$, and $L_2 \approx 10L_1$ (see also Ref. [17]). Experimental values for J vary widely, from 10^{-6} to $10^{-4}\ \mathrm{J\ m^{-2}}$ [18]. With a blood cell radius of approximately $a = 4\mu m$, we compute $\beta \approx 80$, $\bar{L}_2 = 10$, and $\bar{J}$ is in the range $4 - 400$ (as discussed below, we found $\bar{J} = 100$ to provide close agreement with experimental observations of RBC cell shapes). The nematic coherence length is roughly $\xi_N \approx 50$nm and the extrapolation length ξ_S ranges from 10nm to $1\,\mu$m. We take the nematic strength to be $U = 3.4$ (and by Eq. (4), $S = 0.6$), placing the director field well into the nematic phase. The separation of length scales indicated by the dimensionless value $\beta = 80$ is not easily accessed by our numerical approach. We fix $\beta = 50$ for the remainder of the paper, and note that no significant differences were found when varying β from 10 to 50.

The time-scale selected is that in which the viscous stresses balance the bulk elastic stresses (i.e. the Ericksen number is unity $\mathrm{Er} = 1$). This choice is not particularly important given that we seek a relaxation towards an equilibrium configuration. The scaling also results in a dimensionless shear modulus of $E_S^* = (a/L_1)E_S = 1.6$, and $E_D^* = (a/L_1)E_D = 40$. The dimensionless bending stiffness is given by $B^* = B/(aL_1) = 0.0045$. The cost to bend is far smaller than the cost to deform the material in-plane, and henceforth we neglect the bending energy. (Upon its inclusion into the simulations, we found no noticeable differences in the physics but a sizable increase in the computational time required). Our finding that E_S^* is approximately unity indicates that the bulk LC elasticity and membrane elasticity are comparable, so that a substantial relaxation of the RBC is expected upon its introduction into the LC.

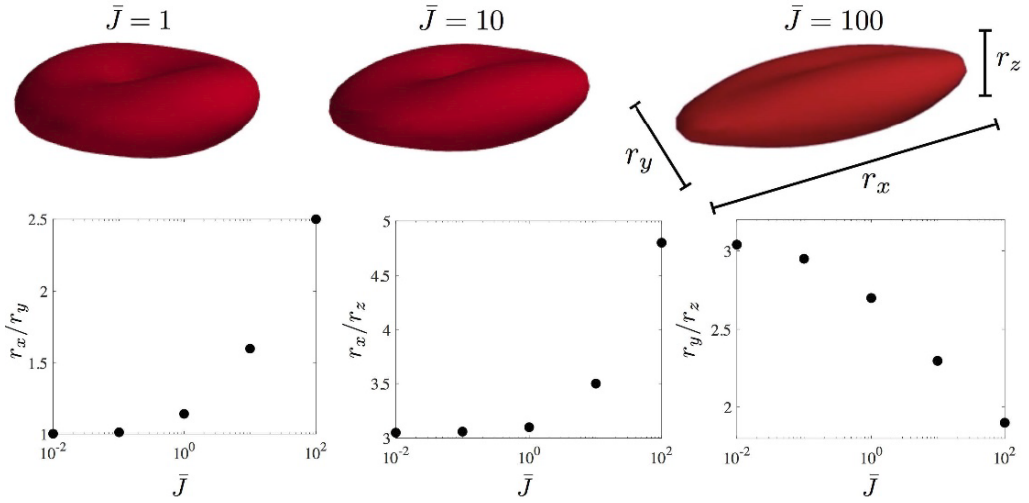

Figure S7: Computed shape metrics of strained RBCs as a function of the dimensionless anchoring energy at the RBC-LC interface.

Though a departure from the physical problem, for tractability, the model described above assumes that the LC is both inside and outside of the cell. Past studies [19, 20] estimate the deformation energy of a LC confined to a spindle-like shape to be $\sim 6K_1 r_y (r_x/r_y)^2$. Assuming that the strained shape of an RBC is spindle-like, for values of r_x/r_y encountered in our work, we predict that our computation overestimates the LC elastic energy by a factor of ~2. We compensate for the presence of LC inside the RBC in our computations by using values of anchoring energy (J) of the LC at the RBC interface corresponding to weak anchoring, with $J \sim 2.5 * 10^{-5}$ J/m^2 ($\bar{J} \sim 100$). Shapes of strained RBCs captured by our computations for the values of $J \sim 2.5 * 10^{-5}$ J/m^2 (Figure S7) are validated by comparison to shapes of RBCs reconstructed through confocal microscopy measurements, as shown in Figure 4. Additionally, from Figure S7, we note that for $J \sim 2.5 * 10^{-5}$ J/m^2, the computed values of aspect ratios ($r_x/r_y \sim 2.5$) are consistent with experimental observations presented in Figure 3. In contrast, the computed shapes of strained RBCs for values of $J \sim 2.5 * 10^{-7}$ J/m^2 ($\bar{J} \sim 1$) are qualitatively different from experimentally observed strained shapes of RBCs. Computations performed with values of $J \sim 2.5 * 10^{-6}$ J/m^2 ($\bar{J} \sim 10$) result in aspect ratios ($r_x/r_y \sim 1.4$) of RBCs that were lower than values obtained in experiments (Figure 3C). We also clarify that the key result of our study is the identification of a high level of cell- to-cell variation in elastic properties; this heterogeneity will not be introduced by the approximations that we have made in describing the coupling of the LC strain to the RBC.

Other equilibrium shapes, found using the simulations using non-physical RBC shear moduli, include that show in Figure S8, where two substantial lobes develop and are separated by a thin, flat region, as described in the main text.

Spatial and temporal discretization:

At every body configuration we relax the director field until it has reached a steady state. Discretizing Eq. (6) with step-size Δt, we advance by

$$\frac{\mathbf{Q}^{n+1} - \mathbf{Q}^n}{\Delta t} = -\left(\mathbf{H}^{(1)}(\mathbf{Q}^{n+1}) + \mathbf{H}^{(2)}(\tilde{\mathbf{Q}})\right), \tag{23}$$

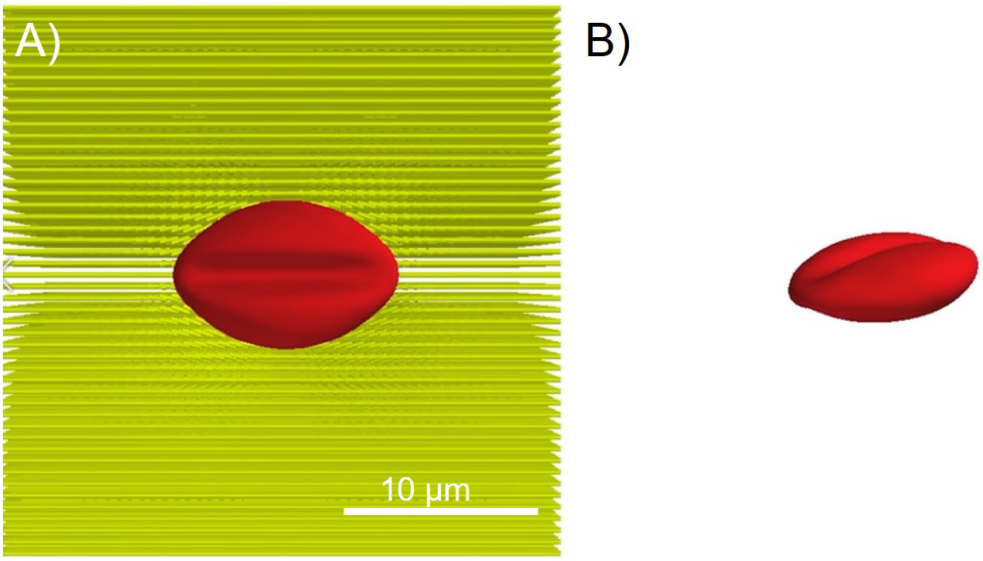

Figure S8: Shapes of strained RBCs computed using a value of the shear modulus of $E_S = 4 * 10^{-5}$ N/m. A) Top view of the strained shape of RBC showing the prominent lobes and neck region. B) Profile view of the strained shape of the RBC shown in A).

where

$$\mathbf{H}^{(1)}(\mathbf{Q}) = -\nabla^2\mathbf{Q} - \bar{L}_2\left[\nabla(\nabla\cdot\mathbf{Q})\right]^{ST} + \beta^2\left(1-\frac{U}{3}\right)\mathbf{Q} + \bar{J}\mathcal{S}_h^n\mathcal{S}_h^{n,*}\mathbf{Q}, \tag{24}$$

$$\mathbf{H}^{(2)}(\mathbf{Q}) = -\beta^2 U\left(\mathbf{Q}^2 - \mathrm{tr}\left(\mathbf{Q}^2\right)\left(\mathbf{Q}+\frac{1}{3}\mathbf{I}\right)\right) - \bar{J}\mathcal{S}_h^n\mathbf{Q}^0. \tag{25}$$

The operations $\mathcal{S}^n$ and $\mathcal{S}^{n,*}$ are discretized spreading and interpolation operators, respectively; they are developed using the original functional form of the discrete delta functions from Ref. [5] which have compact support over a radius of two grid-cells. In the time-stepping shown above we split the molecular field into linear and nonlinear parts, extrapolating for the nonlinear terms using $\tilde{\mathbf{Q}} = 2\mathbf{Q}^n - \mathbf{Q}^{n-1}$. The evolution of $\mathbf{Q}$ is carried out using adaptive time-stepping until $\max_{\mathbf{x}\in\Omega}\|\mathbf{H}\|_\infty \leq 10^{-3}$. The system is solved on a three-dimensional periodic domain with dimensions $(2\pi)^3$ on a regular grid with 96^3 spatial grid-points, using a Fourier spectral decomposition for spatial derivatives. A cross-section of the RBC and the relaxed state of the director field at $t = 0$ are shown in Figure S9, which includes defects appearing at the fore/aft points on the surface. We note that defects can form using the simplified uniaxial $\mathbf{Q}$ tensor model which we employ; the eigenvectors and eigenvalues of the $\mathbf{Q}$ tensor dynamically evolve and the associated scalar order parameter is not fixed but instead is calculated from them.

To relax the shape of the RBC, we solved for the flow field generated by the surface tractions (which includes both the internal elastic forces and the bulk-elastic forces which enter via the Ericksen stress). As we are interested in the equilibrium membrane geometry we neglect anisotropic viscosity. The effects of "back-flow," with elastic bulk energy funneling back into fluid flow, are also negligible for small rotational viscosity, which we've chosen artificially to encourage faster convergence to the equilibrium shape. After computing the quasi-static equilibrium $\mathbf{Q}$, using the same Immersed Boundary technique and spreading operators discussed above (see Ref. [5] for details), we solve the incompressible Stokes equations describing the evolution of the fluid

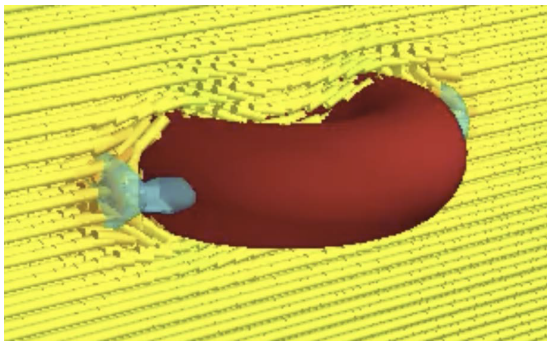

Figure S9: Cross-section of the RBC and the relaxed state of the director field at $t = 0$. Two defects appear at the fore/aft points on the surface; the $S = 0.4$ (scalar order parameter) level set is shown. The RBC relaxes in the direction of the defects to reduce the LC elastic energy, at the cost of RBC elastic energy, until the two are in balance.

velocity field $\boldsymbol{u}$ (and pressure p),

$$-\nabla p + \nabla^2 \boldsymbol{u} + \nabla \cdot \left[\boldsymbol{\sigma}^E + \mathbf{H} : \boldsymbol{\lambda}\right] + \mathcal{S}[\boldsymbol{f}] = \mathbf{0}, \tag{26}$$

$$\nabla \cdot \boldsymbol{u} = 0, \tag{27}$$

from which we advance the body shape via $\boldsymbol{X}_t = \mathcal{S}^*[\boldsymbol{u}]$ using a simple forward-Euler marching scheme. After the boundary has been advanced, we continue again with a relaxation of $\mathbf{Q}$ as described above.

Movie S1: Video showing a 3-D reconstruction of the z-stack images obtained through confocal microscopy.

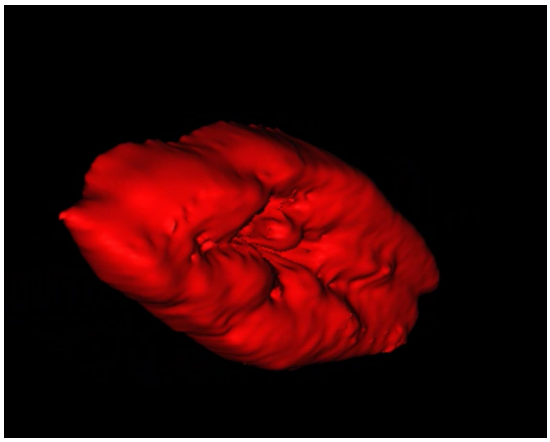

Movie S2: Video showing simulated cross-section of equilibrium RBC shape and LC configuration.

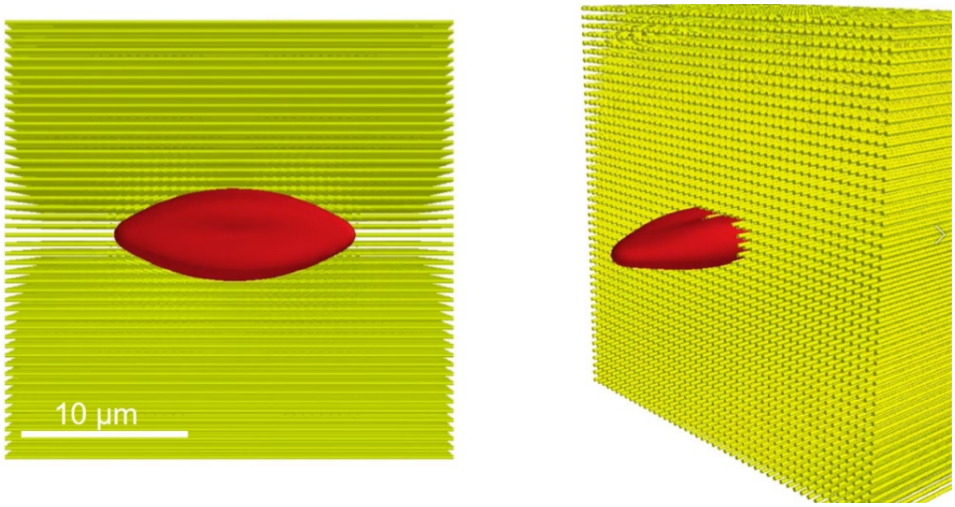

Movie S3: Video showing simulated RBC shapes for $E_S = 4 * 10^{-5}$ N/m.

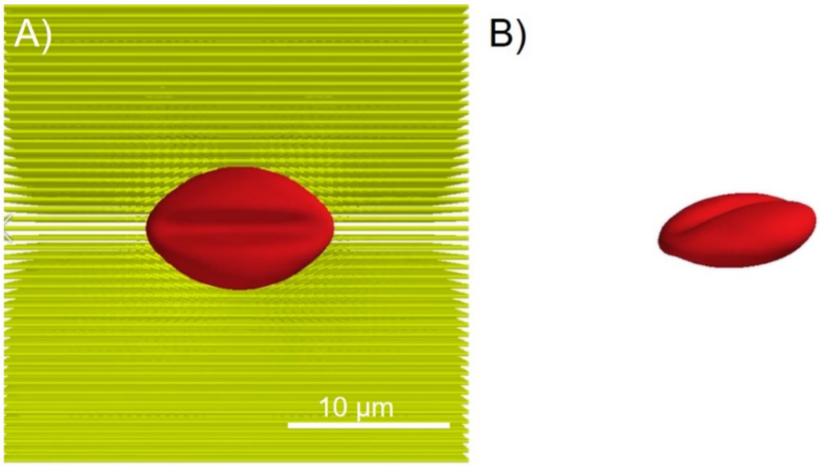

Movie S4: Video (7 fps) showing motion of the nematic-isotropic interface (and the RBC), resulting in the transfer of a RBC from an isotropic region to nematic region of 17.3% DSCG.

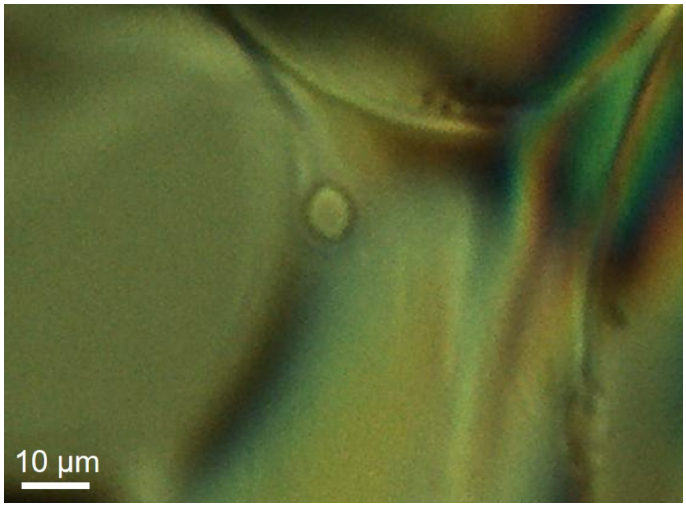

[1] P. G. de Gennes and J. Prost, *The Physics of Liquid Crystals* (Oxford University Press, Oxford, 1995), 2nd ed.

[2] A. M. Sonnet, P. L. Maffettone, and E. G. Virga, J. Non-Newtonian Fluid Mech. **119**, 51 (2004).

[3] H. Stark and T. C. Lubensky, Phys. Rev. E **67**, 061709 (2003).

[4] J. P. Hernández-Ortiz, B. T. Gettelfinger, J. Moreno-Razo, and J. J. de Pablo, J. Chem. Phys. **134**, 134905 (2011).

[5] C. S. Peskin, Acta Numer. **11**, 479 (2002).

[6] B. Thomases and R. D. Guy, in "Computational challenges for simulating strongly elastic flows in biology" *in Complex Fluids in Biological Systems: Experiment, Theory and Computation, S. E. Spagnolie, Ed.* (Springer, New York, 2015), pp. 359–397.

[7] J.-B. Fournier and P. Galatola, Europhys. Lett. **72**, 403 (2005).

[8] V. Tomar, T. F. Roberts, N. L. Abbott, J. P. Hernández-Ortiz, and J. J. De Pablo, Langmuir **28**, 6124 (2012).

[9] R. Skalak, A. Tozeren, R. P. Zarda, and S. Chien, Biophys. J. **13**, 245 (1973).

[10] E. A. Evans, Biophys. J. **13**, 926 (1973).

[11] H. Zhao, A. H. G. Isfahani, L. N. Olson, and J. B. Freund, J. Comput. Phys. **229**, 3726 (2010).

[12] C. Pozrikidis, Annals Biomed. Eng. **31**, 1194 (2003).

[13] D. A. Fedosov, B. Caswell, and G. E. Karniadakis, Biophys. J. **98**, 2215 (2010).

[14] J. B. Freund, Annu. Rev. Fluid Mech. **46**, 67 (2014).

[15] K. Sinha and M. D. Graham, Phys. Rev. E **92**, 042710 (2015).

[16] P.-O. Persson and G. Strang, SIAM Rev. **46**, 329 (2004).

[17] S. Zhou, in *Lyotropic Chromonic Liquid Crystals* (Springer, 2017), pp. 51–75.

[18] O. D. Lavrentovich, Soft Matter **10**, 1264 (2014).

[19] P. Prinsen and P. van der Schoot, Phys. Rev. E **68**, 021701 (2003).

[20] P. C. Mushenheim, J. S. Pendery, D. B. Weibel, S. E. Spagnolie, and N. L. Abbott, PNAS **113**, 5564 (2016).